Materials Chemistry and Physics 318 (2024) 129316

Contents lists available at ScienceDirect

Materials Chemistry and Physics

journal homepage: www.elsevier.com/locate/matchemphys

Influence of Al addition on microstructure and electrochemical behaviour of CrMnFeCoNi high-entropy alloy

Lorea Armendariz [a,*], Lucia Castrillejo [a], Iban Vicario [b], Olaia Gordo-Burgoa [c], Teresa Guraya [a]

[a] Department of Mining & Metallurgical Engineering and Materials Science, Faculty of Engineering of Bilbao (UPV/EHU), 48013, Bilbao, Spain
[b] Manufacturing Processes and Materials Department, Tecnalia, Basque Research and Technology Alliance (BRTA), 48160, Derio, Spain
[c] Mechanical and Manufacturing Department, Faculty of Engineering, Mondragon Unibertsitatea, 20500, Arrasate/Mondragon, Spain

HIGHLIGHTS

- $CrMnFeCoNiAl_x$ HEAs are manufactured through a cost-reduced large-scale process.
- Solid solution strengthening is observed with x = 0.30 Al content.
- Al improves general and pitting corrosion resistance of CrMnFeCoNi alloy.
- The pitting density is reduced with the addition of Al.

ARTICLE INFO

Keywords:
$CrMnFeCoNiAl_x$
High-entropy alloy
Al addition
Induction casting
Microstructure
Corrosion properties

ABSTRACT

To develop new corrosion-resistant materials for structural applications, $CrMnFeCoNiAl_x$ high-entropy alloys (HEAs) are produced via semi-industrial induction casting. The study aimed to investigate the influence of Al content (x = 0–0.3) on both microstructure evolution and corrosion properties of the alloys. X-ray diffraction and scanning electron microscopy (SEM) analysis revealed that all the alloys exhibited a single-phase face-centered cubic structure, with dendritic (Fe, Co, Cr-rich) and interdendritic (Mn, Ni, Al-rich) regions distinguished by elemental segregations. Furthermore, the incorporation of Al atoms into the solid solution led to an increase in the lattice parameter, indicating alloy strengthening. The corrosion resistance of the $CrMnFeCoNiAl_x$ alloy improved with higher Al addition. Electrochemical polarisation tests demonstrated a slight increase in the corrosion potential (E_{corr}) and a significant decrease in the corrosion current density (i_{corr}) upon Al addition. Additionally, slower kinetics for pit nucleation (higher E'_{corr}) were observed, particularly notable for x = 0.3. Analysis of the corroded surfaces revealed a mixed degradation mechanism, involving pitting corrosion and selective dissolution of the interdendritic zone, which decreased as the Al content of the HEA increased. These findings underscore the effectiveness of Al addition in not only enhancing the mechanical properties of the Cantor alloy through solid solution strengthening, but also improving its corrosion resistance.

1. Introduction

The discovery of high-entropy alloys (HEA) by Yeh et al. [1] and Cantor et al. [2] in 2004 revolutionized the landscape of traditional metallurgy. These breakthroughs introduced a novel approach to alloy design, shifting attention towards the central region of the multicomponent phase diagram, away from the edges where conventional alloy development had been focused. Indeed, HEAs are characterised by their complex composition, comprising at least five principal elements in equimolar or near-equimolar proportions ranging from 5% to 35%. These alloys exhibit a unique combination of properties attributed to the interplay of four core effects: high mixing entropy, lattice distortion, sluggish diffusion, and cocktail effect [3]. In particular, the equiatomic, single-phase, face-centered cubic (FCC) CrMnFeCoNi Cantor alloy [2] has garnered significant attention for its exceptional thermodynamic stability and damage tolerance, evidenced by its high fracture toughness and ductility at cryogenic temperatures [4,5]. Moreover, unlike traditional structural steels [6–9], recent studies have highlighted the remarkable resistance of the Cantor alloy to hydrogen embrittlement (HE) [10–12]. Its ability to maintain, or even enhance, strength and

* Corresponding author.
E-mail address: lorea.armendariz@ehu.eus (L. Armendariz).

https://doi.org/10.1016/j.matchemphys.2024.129316
Received 12 February 2024; Received in revised form 4 April 2024; Accepted 8 April 2024
Available online 8 April 2024

ductility in hydrogen-rich environments positions the Cantor alloy as a promising candidate for future structural applications, particularly in industries such as fusion, hydrogen fuel, and energy storage.

However, for HEAs to transition into practical engineering components, it is imperative to explore feasible and scalable production methods suitable for industrial applications. Although a wide range of manufacturing routes have been developed for HEAs [13], most reported studies rely on laboratory-scale fabrication methods [2,5,14]. These methods typically involve the use of high-purity raw materials, are carried out in meticulously controlled atmospheres, and may include subsequent remelting cycles. As a result, the materials produced exhibit high microstructural refinement, minimal impurities, and nearly homogeneous chemical compositions. Nevertheless, extrapolating these findings to HEAs fabricated under conditions typical of real structural component production poses significant challenges.

Moreover, the practical applicability of Cantor alloy has consistently been hindered by its low strength at room temperature [5,14] and limited corrosion resistance in chloride solutions [15,16]. Extensive efforts have been undertaken to address these constraints [17–19]. For instance, strengthening effects resulting from solid solution, the formation of a body-centered cubic (BCC) phase, or the precipitation of intermetallic phases have been achieved by incorporating alloying elements such as Al, Ti, Sn, Zr, Si, and Mg [20]. Notably, the addition of large-sized atoms like Al has been reported to significantly enhance the strength and hardness of various HEAs through solid solution strengthening and the formation of a BCC phase [21–24]. Indeed, depending on the Al content within the CrMnFeCoNiAl system three distinct microstructural regimes have been identified [25,26]. For Al contents below 7–8 at.% an equiaxed, dendritic, single-phase FCC solid solution is observed. With increased Al content, a BCC-rich phase appears along grain boundaries and interdendritic zones. Further addition of Al leads to the transformation of the dendritic FCC phase into a lamella-like structure, with the BCC phase becoming noticeable in inter-side-plate areas. Eventually, for Al contents exceeding 16 at.% a single-phase BCC structure becomes predominant. The transition from a single-phase FCC to a BCC structure has been attributed to a significant increase in the lattice distortion energy with Al addition.

On the other hand, it is widely recognised that Al plays a pivotal role in enhancing the oxidation behaviour of Ni-based alloys [27,28]. However, the influence of Al addition on the corrosion resistance of HEAs in chloride-containing aqueous environments remains a topic of discussion. Some studies have indicated a decrease in corrosion resistance in alloys such as $FeCoNiCrCu_{0.5}Al_x$ (x = 0.5–1.5) [29] and $CoCrFeNiAl_x$ (x = 0–2) [30,31] with increasing Al content, attributed to the formation of a BCC phase. Conversely, other research has reported superior corrosion properties in alloys like $Al_xCoCrFeNi$ (x = 0.3–0.9) [32] and $CoNiVAl_x$ (x = 0–0.3) [33] due to the addition of Al. Hence, considering that corrosion behaviour is influenced by various factors including the testing environment, microstructure, phase composition and processing route of the alloy [34], individual studies tailored to each HEA system are necessary.

The present study has a dual purpose. Firstly, it aims to produce a Cantor HEA using a semi-industrial manufacturing route – specifically, induction melting – in an uncontrolled atmosphere while utilizing ferroalloy feedstock. This approach mirrors real component fabrication conditions, with the goal of reducing fabrication costs and the carbon footprint of the alloy. Secondly, the study seeks to investigate the influence of Al addition on the microstructure and corrosion resistance of the aforementioned semi-industrially manufactured Cantor alloy. To achieve these objectives, $CrMnFeCoNiAl_x$ HEAs with three different Al contents (x = 0, 0.03 and 0.3) were fabricated through a semi-industrial induction-melting process. Microstructural analysis of the HEAs, including lattice parameter determination, was conducted using X-ray diffraction (XRD), optical microscopy (OM), and scanning electron microscopy (SEM) equipped with energy-dispersive X-ray spectroscopy (EDX). Furthermore, the corrosion behaviour was assessed via potentiodynamic polarisation and cyclic polarisation measurements in a 0.6M NaCl aqueous solution. Finally, a comprehensive SEM analysis of the corroded samples was conducted to gain insight into the corrosion mechanisms of the fabricated HEAs.

Table 1
Chemical composition (wt.%) of the raw FeCr ferroalloy used in the present study measured by ICP-MS.

ICP	Cr	Fe	C	S
FeCr	69.35	30.60	0.03	0.02

2. Materials and methods

2.1. Material preparation

Three high-entropy alloys with nominal compositions of CrMnFeCoNiAl_x (where x represents the molar ratio of Al, specifically chosen as x = 0, 0.03, and 0.30) and denoted as Al_x hereafter, were synthesized via induction melting in an air atmosphere at a temperature of 1680°C. A Radyne induction furnace, equipped with an 8-turn coil having an inner diameter of 170 mm and a total length of 290 mm, was employed for alloy preparation. The furnace had a maximum power of 15 kW and operated at a frequency range of 20–60 kHz. The raw materials employed consisted of 30 wt.% Fe and 70 wt.% Cr ferrochrome (complete composition in Table 1), along with pure metals of Mn, Co, Ni and Al. The Al content was intentionally limited to low concentrations (<7 at.%) to maintain the single-phase FCC structure, which is beneficial for corrosion resistance, and to prevent the precipitation of secondary phases that could lead to material embrittlement. 30 kg of each alloy was subsequently cast into a metallic die and solidified at an approximate cooling rate of 3°C/s. Cylindrical ingots with a diameter of 70 mm and a total length of 150 mm were obtained from the as-cast material, and no remelting of the alloys was performed. The actual chemical compositions of the alloys, closely matching the nominal values, were determined using inductively coupled plasma mass spectrometry (ICP-MS) (Table 2). From the as-cast cylindrical ingots, disks with a diameter of 70 mm and a thickness of 8 mm were extracted. Each disk was then cut into three identical pieces using a precision cutting machine Metkon Metacut 251 for microstructural and electrochemical analysis. The entire manufacturing process for the HEAs, including sample extraction, is schematically illustrated in Fig. 1.

2.2. Microstructural characterization

The samples were wet-ground up to 4000 SiC grit paper (5 μm grain size) and mechanically polished using a diamond suspension with 3 μm diameter particles. The microstructures of the samples were etched using Kalling's N°2 chemical etchant. Subsequently, the samples were cleaned with alcohol and deionized water and dried with compressed air. The microstructure and chemical composition of the HEAs were evaluated using an optical microscope (OM) Leica DM400 M and a JEOL JMS-6400 scanning electron microscope (SEM) equipped with an energy-dispersive X-ray analysis (EDX) detector INCA X-sight Serie Si (Li) pentaFET from Oxford. X-ray diffraction (XRD) analysis was performed using a PHILIPS X'PERT PRO X-ray diffractometer with Cu-Kα radiation (λ = 1.5418 Å) with Bragg-Brentano geometry, a working voltage of 40 kV and an operating current of 40 mA. The scanning range was set from 20° to 90° of 2θ values, with a scanning speed of 1°/min. The diffraction patterns were indexed using the PDF-4+ database from the International Centre for Diffraction Data (ICDD). Diffracted peaks were fitted by the WinPLOTR profile fitting procedure, employing a pseudo-Voigt function to determine the lattice parameter of the alloys.

Table 2
Chemical composition (at.%) of the three $CrMnFeCoNiAl_x$ (x = 0, 0.03, 0.30) high-entropy alloys.

Nominal	Al	Cr	Mn	Fe	Co	Ni	C	S
Al_0	0.00	20.00	20.00	20.00	20.00	20.00	–	–
$Al_{0.03}$	0.60	19.88	19.88	19.88	19.88	19.88	–	–
$Al_{0.30}$	5.70	18.87	18.87	18.87	18.87	18.87	–	–
ICP								
Al_0	0.00	19.21	19.41	20.72	19.54	20.96	0.14	0.02
$Al_{0.03}$	0.66	19.30	19.79	20.58	19.50	20.06	0.09	0.02
$Al_{0.30}$	5.68	18.30	18.81	19.58	18.37	19.10	0.14	0.02

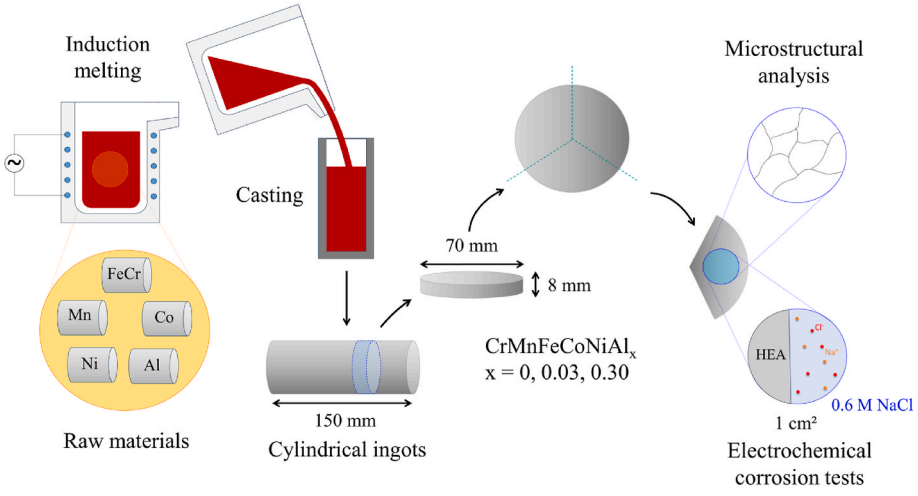

Fig. 1. Schematic representation of the induction melting, casting and characterization process of the $CrMnFeCoNiAl_x$ (x = 0, 0.03, 0.30) high-entropy alloys.

2.3. Corrosion measurements

Potentiodynamic polarisation and cyclic polarisation tests were conducted in an aqueous 0.6M NaCl solution (pH = 6.0) using a three-electrode electrochemical AVESTA-type cell. The cell contained an Ag/AgCl reference electrode inserted in a lugging capillary, a platinum counter electrode, and the specimen as the working electrode. Prior to each corrosion experiment, the samples were wet-ground with a series of SiC papers ranging from 80 to 4000 grit, thoroughly cleaned with alcohol, acetone, and deionized water, and dried using compressed air. During the corrosion experiments, the potential (*E*) was controlled and the current (*I*) was measured using an *Ivium Vertex.One* potentiostat/galvanostat. Current density values (*i*) were obtained by dividing the current by the exposed surface area of the specimen (1 cm^2). Before commencing the tests, the open circuit potential (OCP) was recorded by immersing the samples in the solution for 3300 s.

Potentiodynamic polarisation tests began at an initial potential of −250 mV vs. OCP and were stopped when the current density of the sample reached 1 mA/cm^2. For the cyclic polarisation tests, the sample was cathodically polarized to −250 mV vs. OCP, and a cathodic-to-anodic scan was performed until the current density reached 5 mA/cm^2, after which the scan was reversed back to −250 mV vs. OCP. All tests were conducted at a scan rate of 0.167 mV/s, at room temperature and repeated three times to ensure result repeatability.

2.4. Analysis of corroded surfaces

The surface morphology of the specimens after cyclic polarisation was examined using SEM. EDX compositional analysis was conducted to provide a more detailed characterization of the corroded surfaces. The extent of corrosion was quantified by determining the fraction of corroded area using *ImageJ* software. SEM images were converted to 8-bit format and a thresholding analysis function was applied to differentiate black pixels (indicating corroded areas) and grey pixels (representing the undamaged surface), resulting in a black-and-white binary image. The percentage of corrosion area fraction was estimated by calculating the ratio of the black area to the total area in each SEM binary image. For each tested sample, five images, captured at various magnifications, were analyzed.

3. Results and discussion

3.1. Crystal structure

The XRD patterns of the as-cast $CrMnFeCoNiAl_x$ high-entropy alloys are presented in Fig. 2. Diffracted peaks were indexed to the (111), (200) and (220) crystallographic planes of the prototype FCC phase (PDF: 00-047-1417), consistent with the equiatomic Cantor alloy [2].

The absence of additional peaks in the diffraction patterns shown in Fig. 2a suggests that the original FCC crystal structure has not undergone any phase transformation, such as the precipitation of BCC phase or intermetallic phases, with the addition of Al. Thus, the desired single-phase FCC solid solution of CrMnFeCoNi high-entropy alloy was obtained for all the HEAs manufactured in this work, regardless of the Al content (<6 at.%), consistent with results from previous studies [35]. Furthermore, the clear shift to lower 2θ values of the (111) peak for the $Al_{0.30}$ alloy (Fig. 2b), not observed in $Al_{0.03}$, can be associated with an increase in the lattice constant of the single-phase structure.

Fig. 2c shows the Bragg peaks corresponding to the (111) plane of the FCC structure for each alloy, fitted to a Pseudo Voigt function. The lattice parameter was estimated from the fittings, following Bragg's law for a cubic crystal structure. The evolution of the lattice parameter with Al content is then plotted in Fig. 3a. Firstly, it can be observed that the value determined for Al_0 is 3.6012 Å, which is very close to the original value of 3.59 Å reported by Cantor et al. [2], confirming the accuracy of the fitting. Secondly, the lattice parameter remains nearly constant for $Al_{0.03}$, while an increasing trend is observed with the further addition of aluminium ($Al_{0.3}$). Overall, the values of the lattice constant obtained in

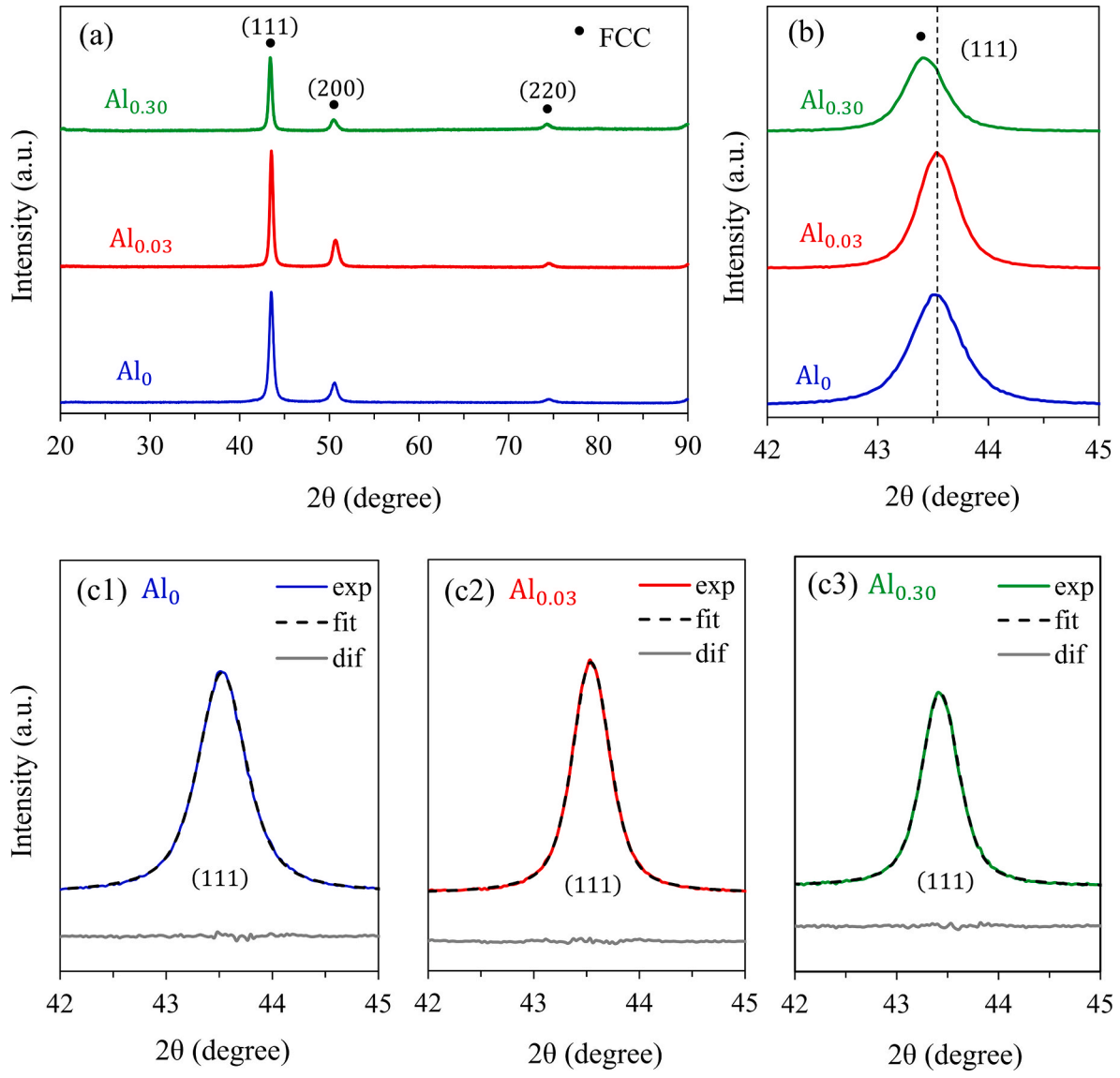

Fig. 2. (a) XRD patterns of as-cast $CrMnFeCoNiAl_x$ (x = 0, 0.03, and 0.30) high-entropy alloys. (b) Magnified pattern showing peak shifting with Al addition. Bragg peaks of the FCC (111) plane reflection fitted with a Pseudo-Voigt function for (c1) Al_0, (c2) $Al_{0.03}$ and (c3) $Al_{0.30}$.

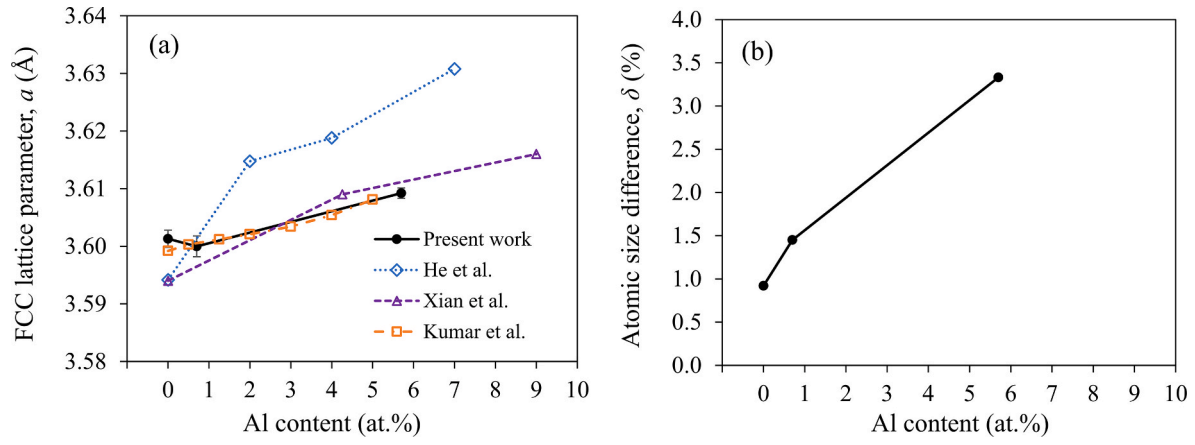

Fig. 3. (a) Evolution of the FCC lattice constant and (b) the atomic size difference parameter (δ) with Al content (at.%) in the $CrMnFeCoNiAl_x$ (x = 0, 0.03, 0.30) high-entropy alloys. Data from Refs. [25,26,35] are included for comparison.

Table 3
Chemical composition (at.%) of the $CrMnFeCoNiAl_x$ (x = 0, 0.03, 0.30) high-entropy alloys measured by EDX.

HEA	Al	Cr	Mn	Fe	Co	Ni
Al_0	–	20.03	19.66	20.29	19.97	20.05
$Al_{0.03}$	1.09	19.74	20.04	20.16	19.54	19.43
$Al_{0.30}$	6.76	18.70	18.59	19.28	18.32	18.35

this work for semi-industrially manufactured $CrMnFeCoNiAl_x$ high-entropy alloys are comparable to those previously reported in the literature for equivalent alloys [25,26,35] obtained through more controlled, small-scale laboratory processes.

The introduction of Al, with a relatively larger atomic radius (143 p.m.) compared to the similar radii of other constituent elements (125–128 p.m.), induces an apparent lattice distortion into the alloy. This phenomenon is explained by the atomic size mismatch effect described by the δ parameter [36]:

$$\delta = \sqrt{\sum_{i=1}^{n} c_i \left(1 - \frac{r_i}{\sum_{j=1}^{n} c_j r_j}\right)^2} \quad (1)$$

where n represents the number of components, c_i and c_j denote the atomic percentages of the i^{th} and j^{th} elements, respectively, and r_i and r_j represent the atomic radius of the i^{th} and j^{th} components.

As observed in Fig. 3b, the introduction of Al atoms into the $CrMnFeCoNiAl_x$ alloy increases the δ values from 0.92% (x = 0) to 3.18% (x = 0.3), indicating a larger lattice distortion. These values meet the criteria for a randomly distributed single-phase solid solution ($\delta \leq$ 6.6%) [36], as evidenced in the XRD patterns (Fig. 2a). Consistent with previous studies, the lattice distortion measured in this work for $Al_{0.3}$ suggests a solid solution strengthening effect - through impeding dislocation motion -, which will result in increased hardness, yield strength and ultimate tensile strength [25,26,35,37].

3.2. Microstructural analysis

The overall chemical composition of each high-entropy alloy was determined through EDX analysis and is documented in Table 3. These values closely align with the desired nominal composition and are similar to those obtained by ICP measurements (Table 2), confirming a successful induction melting process. Optical micrographs depicting the as-cast microstructures are illustrated in Fig. 4. The three alloys under examination exhibit a single-phase dendritic solidification texture, characterised by the absence of significant porosity. EDX mapping (Fig. 5) revealed elemental segregation between dendritic (D) and interdendritic (I) regions in all three alloys. The detailed composition of these regions for Al_0 and $Al_{0.30}$ is given in Table 4. In general, dendrite cores are enriched in Cr, Fe and Co, while interdendritic regions show higher concentrations of Mn, Ni and Al. This behaviour arises from the nature of the solidification process, where elements with higher melting points ($T_{m,Cr}$ = 1907°C, $T_{m,Fe}$ = 1538°C and $T_{m,Co}$ = 1495°C) solidify first, predominantly within dendritic areas. Conversely, elements with lower melting points such as Ni, Mn and Al ($T_{m,Ni}$ = 1455°C, $T_{m,Mn}$ = 1246°C and $T_{m,Al}$ = 660°C), segregate into interdendritic areas, leading to chemical inhomogeneities between these two regions [38]. The phenomenon of segregation between dendritic and interdendritic spaces has been previously documented in as-cast CrMnFeCoNi high-entropy alloys [2,38,39].

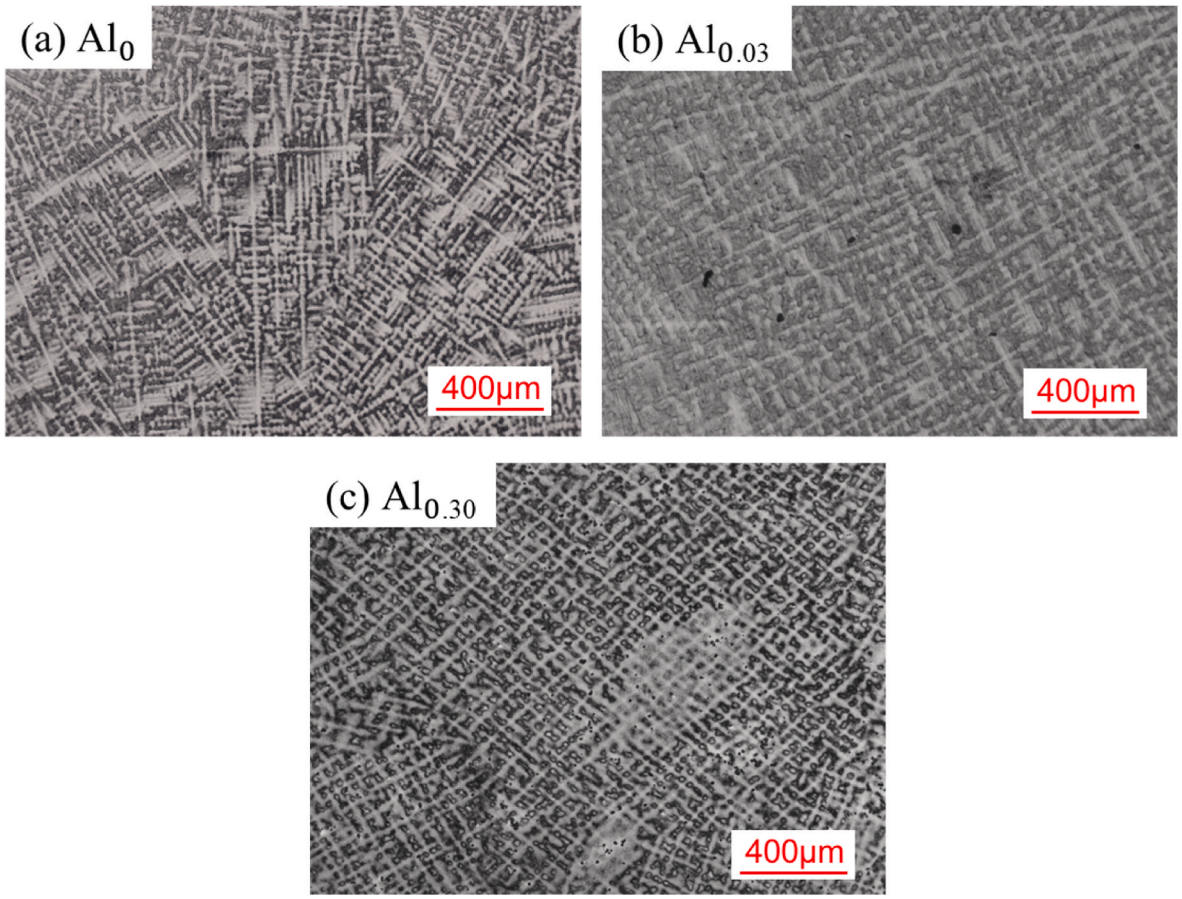

Fig. 4. Optical microscope micrographs of as-cast $CrMnFeCoNiAl_x$ (x = 0, 0.03, 0.30) high-entropy alloys (a) Al_0, (b) $Al_{0.03}$ and (c) $Al_{0.30}$.

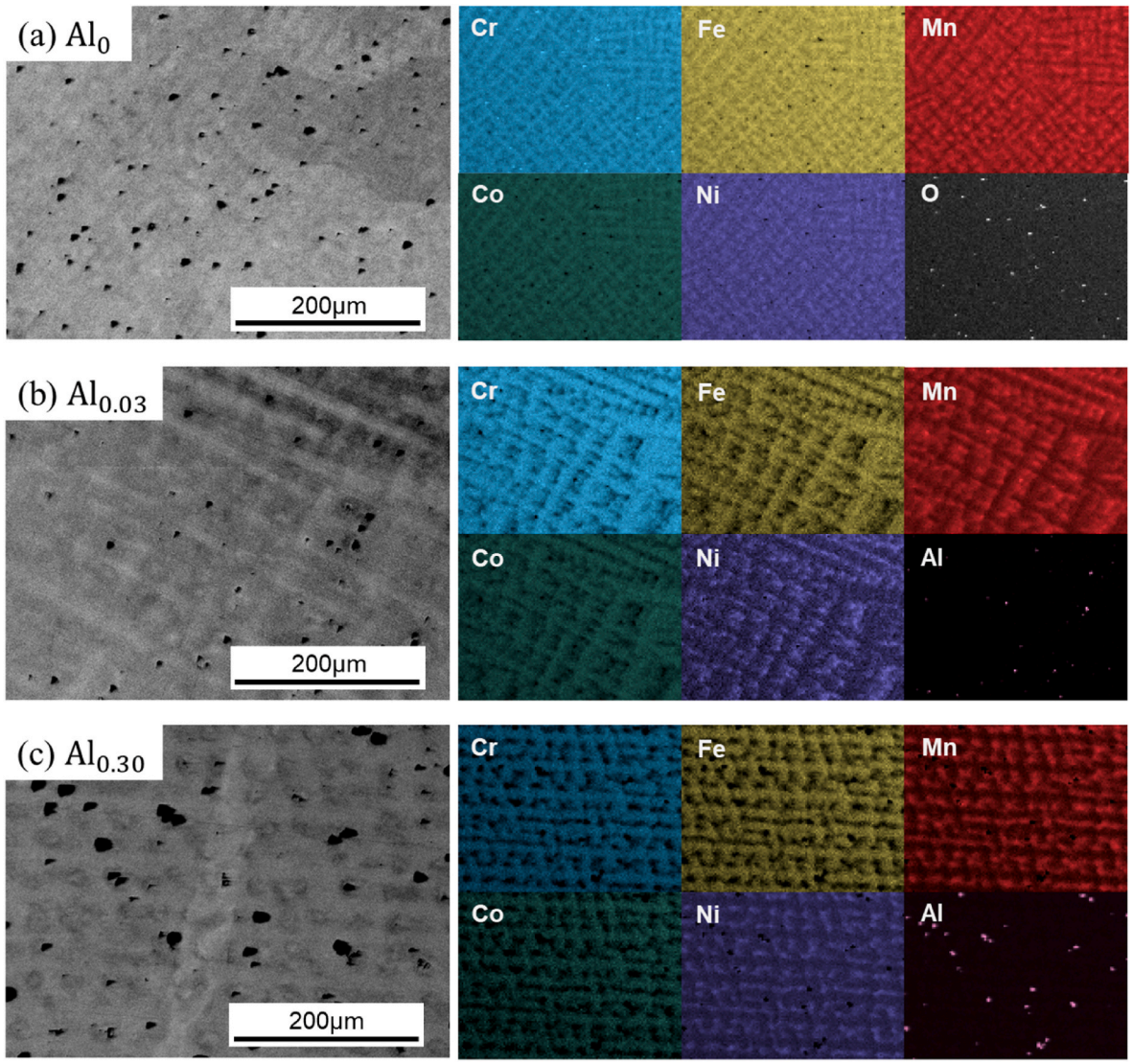

Fig. 5. SEM BSE micrographs and compositional EDX mappings of constituent elements for $CrMnFeCoNiAl_x$ (x = 0, 0.03, 0.30) high-entropy alloys (a) Al_0, (b) $Al_{0.03}$ and (c) $Al_{0.30}$. Dark spots correspond to Mn–Cr oxides in Al_0 and Al–N-rich particles in $Al_{0.03}$ and $Al_{0.30}$ alloys.

Table 4
Chemical composition (at.%) for the dendritic (D) and interdendritic (I) regions of the $CrMnFeCoNiAl_x$ (x = 0 and 0.30) high-entropy alloys measured by EDX.

HEA	Zone	Al	Cr	Mn	Fe	Co	Ni
Al_0	D	–	20.3 ± 0.1	15.1 ± 0.3	23.2 ± 0.4	22.1 ± 0.2	19.3 ± 0.2
	I	–	15.8 ± 0.2	26.2 ± 0.1	15.6 ± 0.6	17.5 ± 0.2	24.9 ± 0.3
$Al_{0.30}$	D	5.0 ± 0.1	19.5 ± 0.3	16.3 ± 0.7	21.2 ± 0.7	19.9 ± 0.3	18.1 ± 0.5
	I	7.2 ± 0.2	13.5 ± 0.7	25.7 ± 0.9	12.6 ± 0.8	15.0 ± 0.7	26.0 ± 1.2

Additionally, near-uniform and randomly distributed inclusions (dark spots) throughout the FCC matrix are observed in backscatter electron micrographs (BSE) (Fig. 5). These particles were analyzed via EDX spot analysis. According to their chemical composition, provided in Table 5, they represent Mn–Cr oxides (potentially $MnCr_2O_4$ [40]) in Al_0 alloy (Fig. 5a) and Al–N-rich particles (potentially AlN [41]) in $Al_{0.03}$ and $Al_{0.30}$ alloys (Fig. 5b and c). However, for a more accurate characterisation of these particles, additional methods such as selected-area electron diffraction (SAED) using transmission electron microscopy (TEM) should be employed. The formation of these particles was associated with the absence of a protective atmosphere, e.g., oxygen contamination, during the casting process [13,16]. It is worth mentioning that, despite the detection of Al-rich particles in EDX maps, the measured Al content in both dendritic and interdendritic regions

Table 5
Chemical composition (at.%) of particles detected in the $CrMnFeCoNiAl_x$ (x = 0, 0.03, 0.30) high-entropy alloys measured by EDX.

HEA	Particle	N	O	Al	Cr	Mn	Fe	Co	Ni
Al_0	Mn–Cr oxide	–	56.15	–	22.27	13.23	2.99	2.68	2.68
$Al_{0.03}$	Al–N-rich particle	53.45	–	43.43	0.28	2.31	–	0.21	0.32
$Al_{0.30}$	Al–N-rich particle	51.04	–	48.28	0.15	0.19	0.17	0.17	–

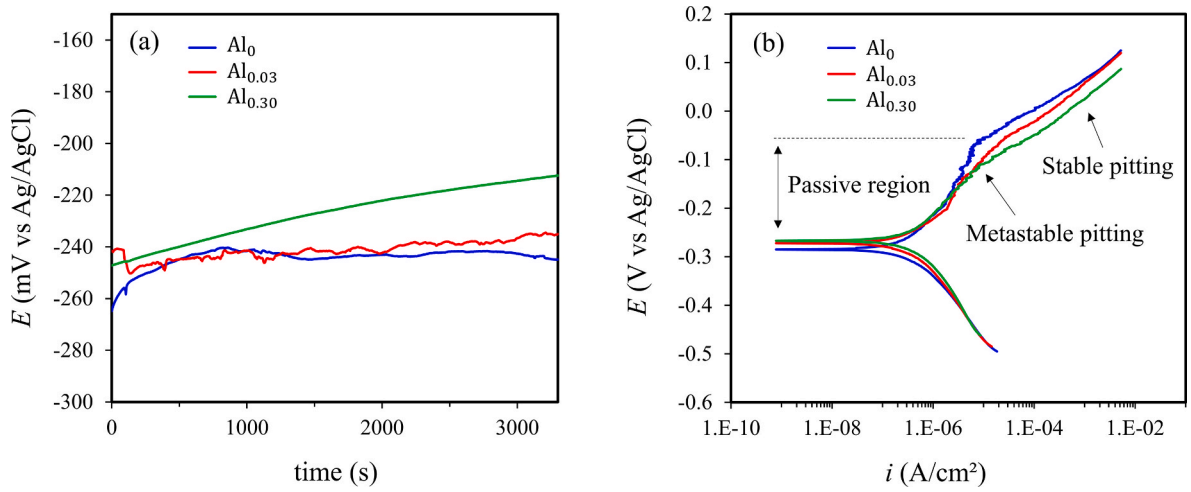

Fig. 6. (a) Open circuit potential (OCP) measurements and (b) potentiodynamic polarisation curves of the $CrMnFeCoNiAl_x$ (x = 0, 0.03, 0.30) high-entropy alloys in a 0.6M NaCl solution at room temperature.

Table 6
Electrochemical parameters of $CrMnFeCoNiAl_x$ (x = 0, 0.03, 0.30) high-entropy alloys obtained by Tafel extrapolation method of the potentiodynamic and cyclic polarisation curves.

HEA	β_c (V/dec)	β_a (V/dec)	E_{corr} ($V_{Ag/AgCl}$)	i_{corr} (A/cm^2)	E_{pit} ($V_{Ag/AgCl}$)	E'_{corr} ($V_{Ag/AgCl}$)
Al_0	0.122	0.104	−0.285	3.82×10^{-7}	−0.133	−0.346
$Al_{0.03}$	0.131	0.145	−0.272	3.69×10^{-7}	−0.145	−0.336
$Al_{0.30}$	0.146	0.104	−0.267	2.86×10^{-7}	−0.134	−0.263

(Table 4) and the increase in lattice parameter for $Al_{0.30}$ (Fig. 3a) suggest that Al atoms were successfully incorporated into the solid solution of the alloys. Moreover, Al–N-rich particles in $Al_{0.03}$ and $Al_{0.30}$ were not detected in XRD diagrams (Fig. 2), suggesting a particle content below the XRD detection limit.

3.3. Corrosion behaviour

Electrochemical experiments were conducted in a 0.6M NaCl solution (pH = 6.0) at room temperature to investigate the influence of Al addition on the corrosion behaviour of $CrMnFeCoNiAl_x$ high-entropy alloy. Open circuit potential (OCP) measurements are depicted in Fig. 6a. While Al_0 and $Al_{0.03}$ alloys exhibit similar open circuit behaviour and rapidly stabilise - within less than 1000 s - at an OCP value of approximately −235 $mV_{Ag/AgCl}$, the curve corresponding to $Al_{0.30}$ alloy reveals a continuous increase in the OCP towards more positive values, reaching around −210 $mV_{Ag/AgCl}$ after approximately 1h, indicating surface passivation.

The potentiodynamic polarisation curves of the $CrMnFeCoNiAl_x$ high-entropy alloy with three different Al contents are presented in Fig. 6b. A gradual shift of the polarisation curves to more noble potentials and lower current densities is observed with the increase in Al content. The electrochemical parameters related to the curves, determined by the Tafel extrapolation method [42], are compiled in Table 6, which includes the cathodic Tafel slope (β_c), anodic tafel slope (β_a), corrosion potential (E_{corr}) and corrosion current density (i_{corr}). It is observed that E_{corr} and i_{corr} are nearly identical for Al_0 and $Al_{0.03}$, suggesting that minor Al additions (approximately 0.66 at.%) may not significantly affect the corrosion resistance of the alloy. However, in line with the trends observed in Fig. 6b, an increase in Al content to approximately 5.68 at.% ($Al_{0.30}$) resulted in a marginal increase in E_{corr} and a 25% decrease in i_{corr}.

The potentiodynamic polarisation results from Fig. 6b also reveal that all three alloys exhibit similar curve shapes, with a small passivation region associated with the formation of a protective oxide film on the metal surface. The recorded current fluctuations along the anodic branch suggest the occurrence of metastable pitting - nucleation and repassivation of pits - in all the alloys [43,44], irrespective of their Al content. This phenomenon aligns with observations in the literature for other high-entropy alloys exposed to saline environments [15,45,46]. Moreover, an increase in current density after the passive region indicates the nucleation of stable pits in all the alloys. Pit growth becomes stable when the potential is sufficiently high - more positive than the pitting potential (E_{pit}) - to sustain the continuous dissolution of the metal [43]. As shown in Table 6, E_{pit} was practically similar in all the alloys, even for the largest Al content of ~5.66 at.%. This finding contradicts a previous study that suggested increased pitting corrosion with Al addition in an $Al_xCoCrFeNi$ Mn-free high-entropy alloy [45]. However, the authors attributed this behaviour to the presence of the BCC phase, which was not found in the high-entropy alloys studied in this work (see Fig. 2a).

To further investigate the susceptibility to pitting and the restoring behaviour of the alloys, cyclic polarisation measurements were conducted, and the resulting curves are shown in Fig. 7. Arrows indicate the direction of the potential scan. The positive hysteresis loop observed in Fig. 7 a, b and c indicate that all three alloys are prone to pitting corrosion. Notably, in each case, E_{corr} is attained during the reverse scan before the hysteresis loop is completed, resulting in more negative second corrosion potential values (E'_{corr}), as displayed in Table 6. This implies that pits continue to grow and propagate during reverse polarisation. However, it is evident that the potential difference between forward and backward corrosion potentials $(\Delta E = E_{corr} - E'_{corr})$ decreases significantly with the increase in Al content and becomes approximately zero for $Al_{0.30}$, suggesting reduced propagation of pitting

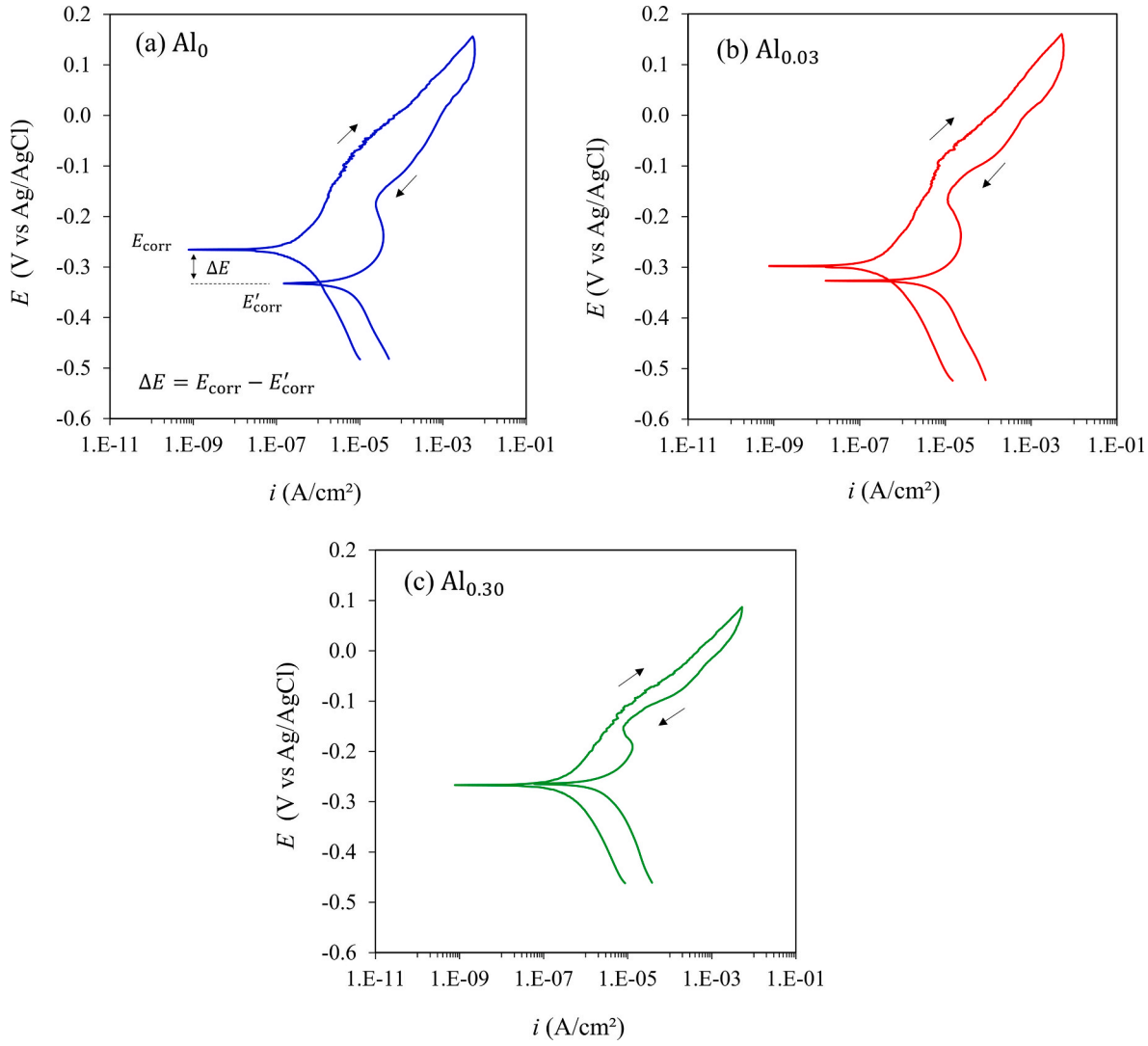

Fig. 7. Cyclic potentiodynamic polarisation curves for $CrMnFeCoNiAl_x$ (x = 0, 0.03, 0.30) high-entropy alloys (a) Al_0, (b) $Al_{0.03}$ and (c) $Al_{0.30}$.

with Al addition. In fact, a smaller area of the hysteresis loop indicates slower growth of the nucleated pits and an enhancement in the restoring ability of the damaged protective layer [47,48].

Overall, the results from the OCP, potentiodynamic, and cyclic polarisation experiments suggest that the addition of an adequate amount of Al can improve the corrosion resistance of the CrMnFeCoNi alloy.

3.4. Analysis of the corroded surfaces

To gain a deeper insight into the influence of Al addition on the corrosion behaviour of $CrMnFeCoNiAl_x$ alloys, the surfaces of the samples after cyclic polarisation were analized using SEM-EDX. Surface morphology and EDX elemental mapping of Al_0, $Al_{0.03}$ and $Al_{0.30}$ are presented in Fig. 8. In Al_0 samples, small spherical pits were predominantly generated in the Ni and Mn enriched areas of the FCC phase (Fig. 8a). Additionally, two regions of darker contrast are observed, corresponding to selective dissolution along the interdendritic region. A similar corrosion mechanism is observed in Fig. 8b for the $Al_{0.03}$ alloy, albeit with considerably lower pit density, shallower pits, and narrower selectively dissolved areas. Regarding the $Al_{0.30}$ alloy, Fig. 8c reveals the absence of significant pitting (Al elemental mapping shows that the circular dark spots correspond to Al-enriched particles) and only a small, dissolved area is observed.

The EDX micrographs presented in Fig. 8 suggest that pits initiated within the interdendritic regions of the Al_0 and $Al_{0.03}$ alloys. The observed interdendritic pitting may be attributed to the elevated Mn content in these areas. Mn is more electrochemically active compared to the other elements, thus the presence of Mn-rich interdendrites alongside Mn-depleted (Cr-rich) dendrites creates an active/noble cell when immersed in a chloride solution, leading to micro-galvanic action. Furthermore, due to the lower Cr content in the interdendritic space, the oxide film may be depleted of chromium in those regions, resulting in compromised performance of the protective layer [49]. The synergistic effect of these phenomena causes chloride ions to preferentially attack Mn-rich (Cr-depleted) areas, leading to the nucleation of pits. Melia et al. [50] observed a similar preferential corrosion morphology along the inter-cellular Mn and Ni-rich regions for an additively manufactured CoCrFeMnNi high-entropy alloy.

To estimate the extent of corrosion observed in Fig. 8, the corroded area fraction, A_c, was determined though image processing of multiple SEM images of the corroded surfaces. Fig. 9a shows examples of the black-and-white binary images generated with *ImageJ* to differentiate the corroded from the undamaged areas. Fig. 9b clearly illustrates a reduction in the corroded area fraction with increasing Al content, suggesting that Al plays a significant role in reducing the alloy's susceptibility to pitting in a 0.6M NaCl solution.

To validate this assumption, Fig. 9c displays the potential difference

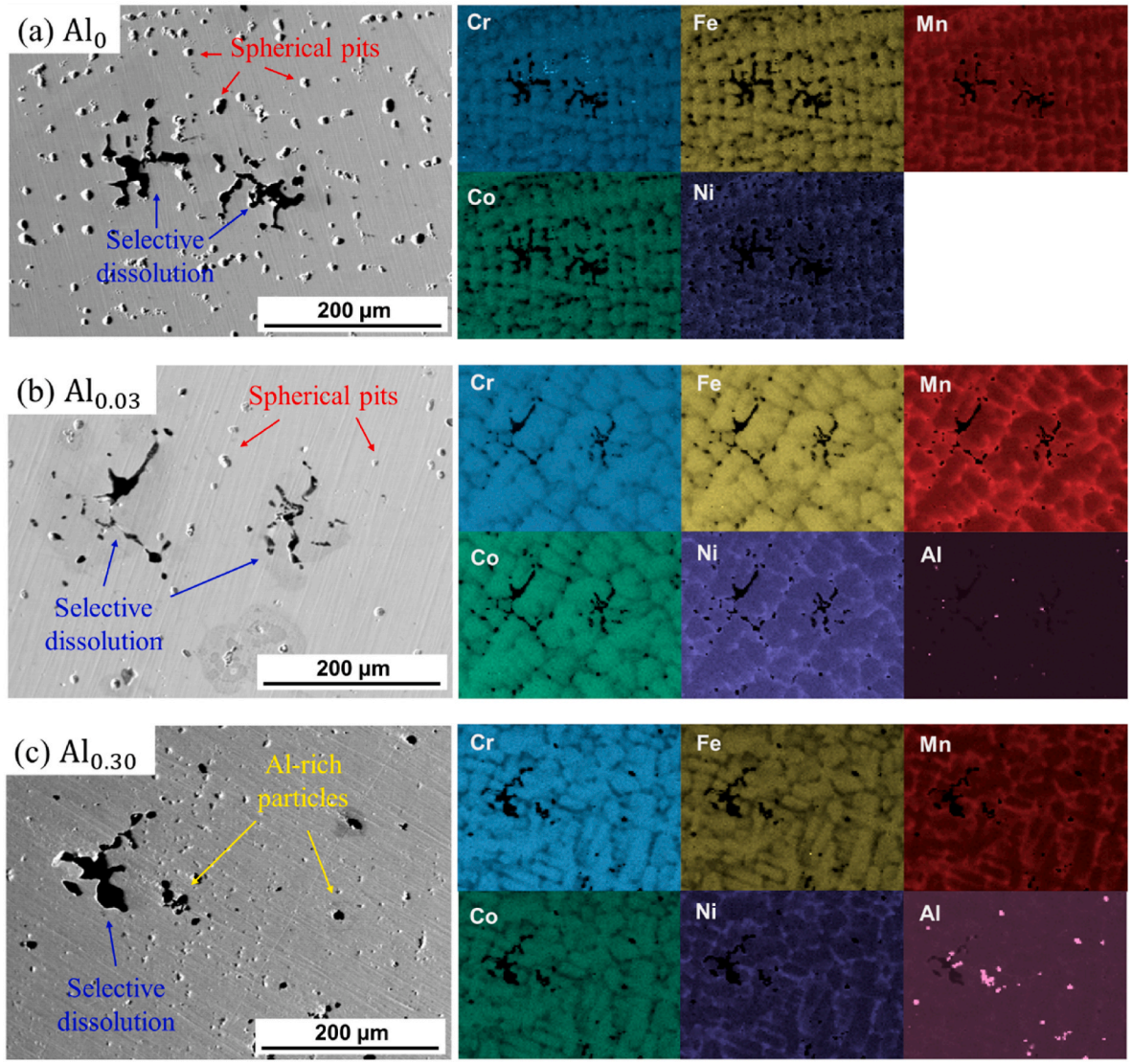

Fig. 8. SEM micrographs and EDX mapping of the corroded surfaces of $CrMnFeCoNiAl_x$ (x = 0, 0.03, 0.30) high-entropy alloys (a) Al_0, (b) $Al_{0.03}$ and (c) $Al_{0.30}$ after cyclic polarisation testing.

between the corrosion potential and the second corrosion potential ($\Delta E = E_{corr} - E'_{corr}$) against the corroded area fraction of each alloy. A linear correlation ($R^2 > 0.99$) is observed, indicating a decrease in the corroded area fraction with narrower ΔE values. The reduction of ΔE is mainly associated with greater resistance to pitting propagation or an enhanced pitting restoring ability of the alloy [42,47,51]. Therefore, this trend confirms that the addition of Al to $CrMnFeCoNiAl_x$ HEA indeed improves the alloy's resistance against pitting corrosion, thereby enhancing its overall corrosion resistance.

4. Conclusions

In the present study, we investigated the influence of aluminum (Al) content on the microstructure and electrochemical corrosion properties of CrMnFeCoNiAlx high-entropy alloys (HEAs). Three alloys with varying Al content (x = 0, 0.03, 0.30) were successfully manufactured via a semi-industrial induction casting process, utilizing ferroalloy feedstock and without a protective atmosphere. Our conclusions are summarized as follows.

- The manufactured HEAs were successfully cast achieving the target nominal compositions and exhibited adequate integrity with no significant porosity.
- Microstructural characterization revealed a single-phase FCC crystal structure in all alloys, with no phase transformation observed with increasing Al content. Dendritic structures were observed, with micro-segregations between dendrites (enriched in Fe, Co, Cr) and interdendritic regions (enriched in Ni, Mn and Al).
- Addition of Al to the Cantor alloy increased the lattice parameter in the $Al_{0.30}$ alloy suggesting a strengthening effect.
- Electrochemical measurements indicated improved corrosion resistance in the $Al_{0.30}$ HEA compared to the Al_0 alloy, characterised by a higher corrosion potential and lower corrosion current.
- Pitting corrosion was observed, along with selectively corroded interdendritic areas. However, the severity of corrosion was reduced in the $Al_{0.30}$ alloy, which exhibited lower pit density, a smaller corroded area fraction, and narrower potential gap, attributed to an improved repassivation ability of the pits.

Overall, the manufactured Al-containing $CrMnFeCoNiAl_x$ HEAs, demonstrated enhanced corrosion resistance combined with the microstructural features that could increase the strength of traditional Cantor

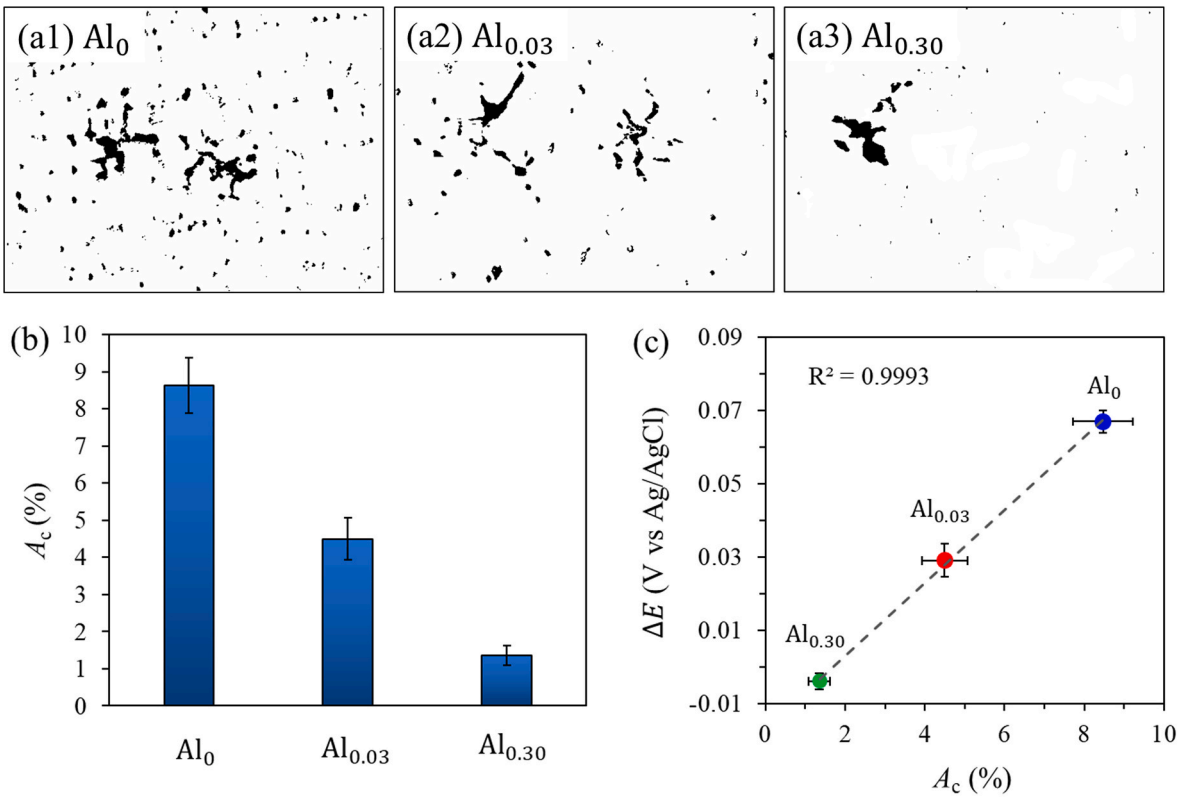

Fig. 9. (a) Corresponding binary images of the SEM micrographs after cyclic polarisation test obtained using *ImageJ* software for $CrMnFeCoNiAl_x$ (x = 0, 0.03, 0.30) high-entropy alloys (a1) Al_0, (a2) $Al_{0.03}$ and (a3) $Al_{0.30}$. (b) Calculated corroded area fractions, A_c (%). (c) $\Delta E = E_{corr} - E'_{corr}$ potential difference as a function of A_c.

alloy.

CRediT authorship contribution statement

Lorea Armendariz: Writing – original draft, Visualization, Validation, Methodology, Investigation, Formal analysis. **Lucia Castrillejo:** Methodology, Investigation, Formal analysis. **Iban Vicario:** Writing – review & editing, Resources, Investigation. **Olaia Gordo-Burgoa:** Resources, Investigation. **Teresa Guraya:** Writing – review & editing, Supervision, Project administration.

Declaration of competing interest

The authors declare that they have no known competing financial interests or personal relationships that could have appeared to influence the work reported in this paper.

Data availability

Data will be made available on request.

Acknowledgements

This work was supported by the Department of Economic Development, Sustainability and Environment of the Basque Government [KK-2022/00064], MCIN/AEI [10.13039/501100011033] and by the European Union NextGenerationEU/PRTR [TED2021-130757A-I00].

References

[1] J.W. Yeh, S.K. Chen, S.J. Lin, J.Y. Gan, T.S. Chin, T.T. Shun, C.H. Tsau, S.Y. Chang, Nanostructured high-entropy alloys with multiple principal elements: novel alloy design concepts and outcomes, Adv. Eng. Mater. 6 (2004) 299–303, https://doi.org/10.1002/adem.200300567.

[2] B. Cantor, I.T.H. Chang, P. Knight, A.J.B. Vincent, Microstructural development in equiatomic multicomponent alloys, Mater. Sci. Eng. A 375–377 (2004) 213–218, https://doi.org/10.1016/j.msea.2003.10.257.

[3] M.H. Tsai, J.W. Yeh, High-entropy alloys: a critical review, Mater Res Lett 2 (2014) 107–123, https://doi.org/10.1080/21663831.2014.912690.

[4] B. Gludovaltz, A. Hohenwarter, D. Catoor, E.H. Chang, E.P. George, R.O. Ritchie, A fracture-resistant high-entropy alloy for cryogenic applications, Science 345 (2014) (1979) 1153–1158, https://doi.org/10.1126/science.1254581.

[5] F. Otto, A. Dlouhý, C. Somsen, H. Bei, G. Eggeler, E.P. George, The influences of temperature and microstructure on the tensile properties of a CoCrFeMnNi high-entropy alloy, Acta Mater. 61 (2013) 5743–5755, https://doi.org/10.1016/j.actamat.2013.06.018.

[6] M.B. Djukic, V.S. Zeravcic, G. Bakic, A. Sedmak, B. Rajicic, Hydrogen embrittlement of low carbon structural steel, Procedia. Mater. Sci. 3 (2014) 1167–1172, https://doi.org/10.1016/j.mspro.2014.06.190.

[7] A. Zafra, L.B. Peral, J. Belzunce, C. Rodríguez, Effect of hydrogen on the tensile properties of 42CrMo4 steel quenched and tempered at different temperatures, Int. J. Hydrogen Energy 43 (2018) 9068–9082, https://doi.org/10.1016/j.ijhydene.2018.03.158.

[8] T. Depover, D. Pérez Escobar, E. Wallaert, Z. Zermout, K. Verbeken, Effect of hydrogen charging on the mechanical properties of advanced high strength steels, Int. J. Hydrogen Energy 39 (2014) 4647–4656, https://doi.org/10.1016/j.ijhydene.2013.12.190.

[9] V. Arniella, A. Zafra, G. Álvarez, J. Belzunce, C. Rodríguez, Comparative study of embrittlement of quenched and tempered steels in hydrogen environments, Int. J. Hydrogen Energy 47 (2022) 17056–17068, https://doi.org/10.1016/j.ijhydene.2022.03.203.

[10] Y. Zhao, D.H. Lee, M.Y. Seok, J.A. Lee, M.P. Phaniraj, J.Y. Suh, H.Y. Ha, J.Y. Kim, U. Ramamurty, J. il Jang, Resistance of CoCrFeMnNi high-entropy alloy to gaseous hydrogen embrittlement, Scr Mater 135 (2017) 54–58, https://doi.org/10.1016/j.scriptamat.2017.03.029.

[11] H. Luo, W. Lu, X. Fang, D. Ponge, Z. Li, D. Raabe, Beating hydrogen with its own weapon: Nano-twin gradients enhance embrittlement resistance of a high-entropy alloy, Mater. Today 21 (2018) 1003–1009, https://doi.org/10.1016/j.mattod.2018.07.015.

[12] H. Luo, Z. Li, D. Raabe, Hydrogen enhances strength and ductility of an equiatomic high-entropy alloy, Sci. Rep. 7 (2017), https://doi.org/10.1038/s41598-017-10774-4.

[13] Y. Zhang, Q. Xing, High entropy alloys: manufacturing routes, in: Encyclopedia of Materials: Metals and Alloys, Elsevier, 2022, pp. 327–338, https://doi.org/10.1016/B978-0-12-803581-8.12123-X.

[14] A. Gali, E.P. George, Tensile properties of high- and medium-entropy alloys, Intermetallics 39 (2013) 74–78, https://doi.org/10.1016/j.intermet.2013.03.018.

[15] C.W. Lu, Y.S. Lu, Z.H. Lai, H.W. Yen, Y.L. Lee, Comparative corrosion behavior of Fe50Mn30Co10Cr10 dual-phase high-entropy alloy and CoCrFeMnNi high-entropy alloy in 3.5 wt% NaCl solution, J. Alloys Compd. 842 (2020), https://doi.org/10.1016/j.jallcom.2020.155824.
[16] Z. Xu, H. Zhang, X. Du, Y. He, H. Luo, G. Song, L. Mao, T. Zhou, L. Wang, Corrosion resistance enhancement of CoCrFeMnNi high-entropy alloy fabricated by additive manufacturing, Corros Sci 177 (2020) 108954, https://doi.org/10.1016/j.corsci.2020.108954.
[17] D. Banik, B. Bhushan, S. Mukherjee, J. Bhagyaraj, H. Fujiwara, K. Ameyama, K. Mondal, Effect of harmonic structure on the electrochemical behavior of high entropy Cantor alloy in NaCl solution, Mater. Chem. Phys. 298 (2023), https://doi.org/10.1016/j.matchemphys.2023.127414.
[18] Z. Szklarz, J. Lekki, P. Bobrowski, M.B. Szklarz, Ł. Rogal, The effect of SiC nanoparticles addition on the electrochemical response of mechanically alloyed CoCrFeMnNi high entropy alloy, Mater. Chem. Phys. 215 (2018) 385–392, https://doi.org/10.1016/j.matchemphys.2018.05.056.
[19] J. Chen, Z. Yao, X. Wang, Y. Lu, X. Wang, Y. Liu, X. Fan, Effect of C content on microstructure and tensile properties of as-cast CoCrFeMnNi high entropy alloy, Mater. Chem. Phys. 210 (2018) 136–145, https://doi.org/10.1016/j.matchemphys.2017.08.011.
[20] Z. Zeng, M. Xiang, D. Zhang, J. Shi, W. Wang, X. Tang, W. Tang, Y. Wang, X. Ma, Z. Chen, W. Ma, K. Morita, Mechanical properties of Cantor alloys driven by additional elements: a review, J. Mater. Res. Technol. 15 (2021) 1920–1934, https://doi.org/10.1016/j.jmrt.2021.09.019.
[21] W.R. Wang, W.L. Wang, S.C. Wang, Y.C. Tsai, C.H. Lai, J.W. Yeh, Effects of Al addition on the microstructure and mechanical property of AlxCoCrFeNi high-entropy alloys, Intermetallics 26 (2012) 44–51, https://doi.org/10.1016/j.intermet.2012.03.005.
[22] Y. Gan, S. Duan, Y. Mo, Y. Dong, J. Yi, Y. Hu, Effects of Al addition on the microstructure and mechanical properties of AlxCoCrFeNi2.1 high-entropy alloys, Intermetallics 166 (2024), https://doi.org/10.1016/j.intermet.2023.108172.
[23] P. wei Wang, X. Li, K. Wang, B. Malomo, L. Yang, Tailoring microstructures and properties in Co-free FeNiCrCuAl high entropy alloys by Al addition, Intermetallics 166 (2024), https://doi.org/10.1016/j.intermet.2023.108175.
[24] Z. Tang, M.C. Gao, H. Diao, T. Yang, J. Liu, T. Zuo, Y. Zhang, Z. Lu, Y. Cheng, Y. Zhang, K.A. Dahmen, P.K. Liaw, T. Egami, Aluminum alloying effects on lattice types, microstructures, and mechanical behavior of high-entropy alloys systems, JOM 65 (2013) 1848–1858, https://doi.org/10.1007/s11837-013-0776-z.
[25] J.Y. He, W.H. Liu, H. Wang, Y. Wu, X.J. Liu, T.G. Nieh, Z.P. Lu, Effects of Al addition on structural evolution and tensile properties of the FeCoNiCrMn high-entropy alloy system, Acta Mater. 62 (2014) 105–113, https://doi.org/10.1016/j.actamat.2013.09.037.
[26] X. Xian, Z.H. Zhong, L.J. Lin, Z.X. Zhu, C. Chen, Y.C. Wu, Tailoring strength and ductility of high-entropy CrMnFeCoNi alloy by adding Al, Rare Met. 41 (2022) 1015–1021, https://doi.org/10.1007/s12598-018-1161-4.
[27] V. Firouzdor, K. Sridharan, G. Cao, M. Anderson, T.R. Allen, Corrosion of a stainless steel and nickel-based alloys in high temperature supercritical carbon dioxide environment, Corros Sci 69 (2013) 281–291, https://doi.org/10.1016/j.corsci.2012.11.041.
[28] S. Ma, Q. Ding, X. Wei, Z. Zhang, H. Bei, The effects of alloying elements Cr, Al, and Si on oxidation Behaviors of Ni-based Superalloys, Materials 15 (2022), https://doi.org/10.3390/ma15207352.
[29] B.Y. Li, K. Peng, A.P. Hu, L.P. Zhou, J.J. Zhu, D.Y. Li, Structure and properties of FeCoNiCrCu0.5Alx high-entropy alloy, Trans. Nonferrous Metals Soc. China 23 (2013) 735–741, https://doi.org/10.1016/S1003-6326(13)62523-6.
[30] Y. Garip, N. Ergin, O. Ozdemir, Resistance sintering of CoCrFeNiAlx (x = 0.7, 0.85, 1) high entropy alloys: microstructural characterization, oxidation and corrosion properties, J. Alloys Compd. 877 (2021), https://doi.org/10.1016/j.jallcom.2021.160180.
[31] M. Izadi, M. Soltanieh, S. Alamolhoda, S.M.S. Aghamiri, M. Mehdizade, Microstructural characterization and corrosion behavior of AlxCoCrFeNi high entropy alloys, Mater. Chem. Phys. 273 (2021), https://doi.org/10.1016/j.matchemphys.2021.124937.
[32] Y. Qiu, M.A. Gibson, H.L. Fraser, N. Birbilis, Corrosion characteristics of high entropy alloys, Mater. Sci. Technol. 31 (2015) 1235–1243, https://doi.org/10.1179/1743284715Y.0000000026.
[33] Z. Pan, H. Luo, Q. Zhao, H. Cheng, Y. Wei, X. Wang, B. Zhang, X. Li, Tailoring microstructure and corrosion behavior of CoNiVAlx medium entropy alloys via Al addition, Corros Sci 207 (2022), https://doi.org/10.1016/j.corsci.2022.110570.
[34] Y. Shi, B. Yang, P.K. Liaw, Corrosion-resistant high-entropy alloys: a review, Metals 7 (2017), https://doi.org/10.3390/met7020043.
[35] J. Kumar, A. Linda, M. Sadhasivam, K.G. Pradeep, N.P. Gurao, K. Biswas, The effect of Al addition on solid solution strengthening in CoCrFeMnNi: experiment and modelling, Acta Mater. 238 (2022), https://doi.org/10.1016/j.actamat.2022.118208.
[36] X. Yang, Y. Zhang, Prediction of high-entropy stabilized solid-solution in multi-component alloys, Mater. Chem. Phys. 132 (2012) 233–238, https://doi.org/10.1016/j.matchemphys.2011.11.021.
[37] J. Kumar, N. Kumar, S. Das, N.P. Gurao, K. Biswas, Effect of Al addition on the microstructural evolution of equiatomic CoCrFeMnNi alloy, Trans. Indian Inst. Met. 71 (2018) 2749–2758, https://doi.org/10.1007/s12666-018-1443-4.
[38] M. Laurent-Brocq, A. Akhatova, L. Perrière, S. Chebini, X. Sauvage, E. Leroy, Y. Champion, Insights into the phase diagram of the CrMnFeCoNi high entropy alloy, Acta Mater. 88 (2015) 355–365, https://doi.org/10.1016/j.actamat.2015.01.068.
[39] G.A. Salishchev, M.A. Tikhonovsky, D.G. Shaysultanov, N.D. Stepanov, A. V. Kuznetsov, I.V. Kolodiy, A.S. Tortika, O.N. Senkov, Effect of Mn and V on structure and mechanical properties of high-entropy alloys based on CoCrFeNi system, J. Alloys Compd. 591 (2014) 11–21, https://doi.org/10.1016/j.jallcom.2013.12.210.
[40] L. Li, L. Wang, M. Zhang, Q. Huang, Formation of Mn-Cr mixed oxide nanosheets with enhanced lithium storage properties, RSC Adv. 8 (2018) 29670–29677, https://doi.org/10.1039/c8ra04868a.
[41] U. Betke, A. Lieb, F. Scheffler, M. Scheffler, Manufacturing of reticulated open-cellular aluminum nitride ceramic foams from aqueous AlN suspensions, Adv. Eng. Mater. 19 (2017), https://doi.org/10.1002/adem.201600660.
[42] W.S. Tait, Electrochemical corrosion basics, in: Handbook of Environmental Degradation of Materials, third ed., Elsevier Inc., 2018, pp. 97–115, https://doi.org/10.1016/B978-0-323-52472-8.00005-8.
[43] P.C. Pistorius, G.T. Burstein, Aspects of the Effects of Electrolyte Composition on the Occurrence of Metastable Pitting on Stainless Steel, 1994.
[44] P.C. Pistorius, G.T. Burstein, Growth of Corrosion Pits on Stainless Steel in Chloride Solution Containing Dilute Sulphate, 1992.
[45] Y. Shi, B. Yang, X. Xie, J. Brechtl, K.A. Dahmen, P.K. Liaw, Corrosion of AlxCoCrFeNi high-entropy alloys: Al-content and potential scan-rate dependent pitting behavior, Corros Sci 119 (2017) 33–45, https://doi.org/10.1016/j.corsci.2017.02.019.
[46] Y.L. Chou, Y.C. Wang, J.W. Yeh, H.C. Shih, Pitting corrosion of the high-entropy alloy Co1.5CrFeNi1.5Ti0.5Mo0.1 in chloride-containing sulphate solutions, Corros Sci 52 (2010) 3481–3491, https://doi.org/10.1016/j.corsci.2010.06.025.
[47] Q. Sun, K. Chen, Potential difference of cyclic polarization curve of an aircraft al alloy: ΔE (Esec,corr – Ecorr), J. Electrochem. Sci. Eng. 11 (2020) 140–147, https://doi.org/10.33961/jecst.2019.00507.
[48] S. Esmailzadeh, M. Aliofkhazraei, H. Sarlak, Interpretation of cyclic potentiodynamic polarization test results for study of corrosion behavior of metals: a review, Protect. Met. Phys. Chem. Surface 54 (2018) 976–989, https://doi.org/10.1134/S207020511805026X.
[49] H. Torbati-Sarraf, M. Shabani, P.D. Jablonski, G.J. Pataky, A. Poursaee, The influence of incorporation of Mn on the pitting corrosion performance of CrFeCoNi High Entropy Alloy at different temperatures, Mater. Des. 184 (2019), https://doi.org/10.1016/j.matdes.2019.108170.
[50] M.A. Melia, J.D. Carroll, S.R. Whetten, S.N. Esmaeely, J. Locke, E. White, I. Anderson, M. Chandross, J.R. Michael, N. Argibay, E.J. Schindelholz, A.B. Kustas, Mechanical and corrosion properties of additively manufactured CoCrFeMnNi high entropy alloy, Addit. Manuf. 29 (2019), https://doi.org/10.1016/j.addma.2019.100833.
[51] B.E. Wilde, A critical appraisal of some popular laboratory electrochemical tests for predicting the localized corrosion resistance of stainless alloys in sea water, Corrosion 28 (1972) 283–291, https://doi.org/10.5006/0010-9312-28.8.283.